High-Fidelity Computational Aerodynamics of the Elytron 4S UAV

Patricia Ventura Díaz
Science & Technology Corporation
NASA Ames Research Center
Moffett Field, California

Seokkwan Yoon
NASA Advanced Supercomputing Division
NASA Ames Research Center
Moffett Field, California

Colin R. Theodore
Aeromechanics Office
NASA Ames Research Center
Moffett Field, California

ABSTRACT

High-fidelity Computational Fluid Dynamics (CFD) have been carried out for the Elytron 4S Unmanned Aerial Vehicle (UAV), also known as the converticopter "proto12". It is the scaled wind tunnel model of the Elytron 4S, an Urban Air Mobility (UAM) concept, a tilt-wing, box-wing rotorcraft capable of Vertical Take-Off and Landing (VTOL). The three-dimensional unsteady Navier-Stokes equations are solved on overset grids employing high-order accurate schemes, dual-time stepping, and a hybrid turbulence model using NASA's CFD code OVERFLOW. The Elytron 4S UAV has been simulated in airplane mode and in helicopter mode.

INTRODUCTION

Multi-rotor Unmanned Aerial Vehicles (UAVs) have grown very popular over the last decade. Their capacity to hover and to perform Vertical Take-Off and Landing (VTOL), together with their great maneuverability, can be used in a wide range of applications such as human and cargo transportation, delivery systems, surveillance missions, and disaster relief. Moreover, UAVs' easy access to the general public and their highly automated control systems ensure a future sky with more and more UAVs.

Nevertheless, multiple rotary-wing UAVs suffer from low aerodynamic performance and sound levels that can be above a person's comfortable noise threshold. While low-fidelity design tools can be used in the first stages of the conception of a UAV, high-fidelity Computational Fluid Dynamics (CFD) methods are necessary to visualize and to understand the complex aerodynamics that take place in multi-rotor configurations where multiple rotors and the fuselage interact due to the close proximity between components. Moreover, accurate prediction of rotorcraft aerodynamics continues to be challenging as the flows are inherently unsteady, nonlinear, and complex. For instance, a rotor blade can encounter the tip vortices from previous blades, producing one of the main sources of noise in rotorcraft: Blade Vortex Interaction (BVI) noise. BVI causes a rapid change in the loading of the blade and generates a highly directional impulsive noise. Predictions are even more difficult when there are aerodynamic interactions between the rotors, the wings, and the fuselage. High-fidelity CFD may offer an advantage over low-fidelity tools when investigations of interactional aerodynamics in multi-rotor vehicles are required and can also provide information to calibrate low-fidelity design tools to account for the aerodynamic interactions.

Presented at the AHS Meeting. San Francisco, California, USA, January 16–19, 2018.

Previous studies of quadrotor UAVs, where four rotors are placed diagonally opposed on an X-shaped airframe and rotate clock-wise (CW) and counter-clock-wise (CCW) for torque cancellation, demonstrated the rotor-fuselage and rotor-rotor aerodynamic interactions (Ref. 1). The effects of weather on a hovering quadcopter were studied in (Ref. 2). Also, in (Ref. 2), simulations of forward flight of a hybrid quadcopter showed that undermounting the fore rotors greatly improves forward thrust.

Fig. 1. Elytron 4S UAV in the US Army 7x10 subsonic wind tunnel at NASA Ames Research Center.

More recently, the concept of Urban Air Mobility (UAM) has been mentioned by both large and small private high-tech companies like Uber, Airbus, and Converticopter, asserting that commute time would be drastically reduced by using UAM vehicles (popularly known as "flying cars"). UAM vehicles will be autonomous and use electric or hybrid propulsion, will transport a small number of passengers from one point in a city to another in a short time, avoiding all ground traffic, and will have the capacity of VTOL, eliminating the need for big infrastructure such as long runways. Their rechargeable batteries promise a greener future for aviation. New Air Traffic Management (ATM) efforts at NASA have

the potential to provide the "flying roads" and manage the traffic of UAM vehicles in big cities.

Still, UAM has to ensure safe, quiet, and efficient vehicles in order to be able to fly in our cities. The objective of the present work is to demonstrate a high-fidelity computational simulation capability to study the aerodynamics of the innovative design of the Elytron 4S UAV; see figure 1 for a picture of the model in the US Army 7x10 subsonic wind tunnel at NASA Ames Research Center. The Elytron 4S UAV is the UAV-scaled model of the UAM vehicle concept, the Elytron 4S. The Elytron 4S UAV - or Elytron for short - is simulated in order to analyze the flow structures and the stability of this configuration.

The Elytron design combines three sets of wings: a single tilt-wing in central position with the prop-rotors mounted on it and two pairs of fixed wings. The fixed wings are split into a forward pair and an aft pair that are joined by winglets, which make use of the joined wing concept, and by a vertical empennage to the fuselage; Figure 2 shows the components. By splitting the wings apart, the design tries to reduce any interference with the thrust of the prop-rotors. The counter-rotating prop-rotors allow for torque cancellation. The tilt-wings can tilt 90°in order to perform VTOL or "helicopter mode". During forward flight or "airplane mode" the tilt angle is 0°. The nose fan is placed in the front of the vehicle for pitch control and better load distribution during VTOL.

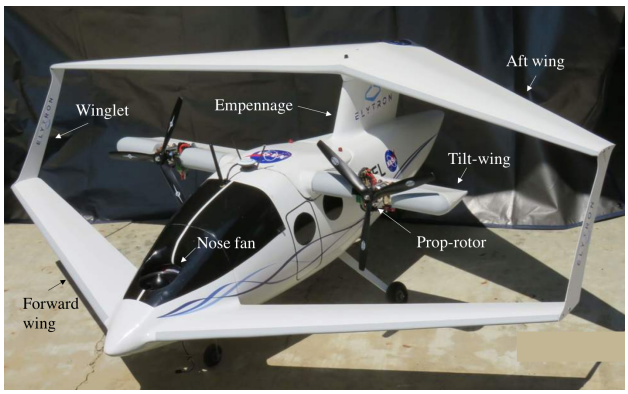

Fig. 2. Elytron 4S UAV components.

The classical monoplane configuration is well known, and the wing design has been improved and optimized, reaching unprecedented levels of efficiency. However, increasing globalization will make existing airplanes inadequate and environmentally unsustainable at some point in the future. The joined wing concept has an interconnected wing that forms a complex over-constrained system, with substantial increase in the design space and allowing more options in terms of aerodynamics, flight mechanincs, engine integration, aeroelasticity, etc. This gives the possibility of finding a *far better* optimum than with traditional designs (Ref. 3). Actually, a hundred years ago, Prandtl introduced the concept of "best wing system" and showed that a box-wing presents the lowest induced drag among wing systems that have the same wingspan, total height, and lift. The Elytron, as mentioned in the previous paragraph, has a joined wing: the forward and aft wings are joined together by winglets, forming a "box-wing". Theoretically, the joined wing of the Elytron should decrease the induced drag. In the results section we will see that this is partially true: some configurations and flight conditions do indeed reduce the wing-tip vortices.

NUMERICAL APPROACH

The flow solver used in this study is NASA's OVERFLOW (Refs. 4, 5) CFD solver. OVERFLOW is a finite-difference, structured overset grid, high-order accurate Navier-Stokes flow solver. NASA's Chimera Grid Tools (CGT) (Ref. 6) overset grid generation software is used for generating the overset grids of the complete vehicles. Body-fitted curvilinear near-body (NB) grids are generated using CGT. The computational domain is completed with the generation of Cartesian off-body (OB) grids, that are automatically generated prior to grid assembly using the Domain Connectivity Framework (DCF) in OVERFLOW-D mode. The current time-accurate approach consists of an inertial coordinate system where near-body curvilinear O-grids for the rotor blades rotate through the fixed off-body Cartesian grid system.

Overset Grid Generation

The overset grid generation procedure using CGT can be divided into the following steps: geometry processing, surface grid generation, volume grid generation, and domain connectivity (Ref. 7).

The geometry is usually obtained from a Computer Aided Design (CAD) model or a 3D-scanning point cloud. Once the geometry is processed as a triangulation reference surface, overlapping hyperbolic and algebraic surface grids are generated using featured curves. The generation of surface grids is the step that requires the most manual effort and experience from the user.

With sufficient overlap between surface grids, the volume grids can be created easily with hyperbolic marching methods out to a fixed distance from the surface. Such methods provide orthogonal grids with tight clustering characteristics at the wall, which is essential for accurately capturing the boundary layer in viscous flow computations. The distance is chosen such that the outer boundaries of the near-body volume grids are well clear of the boundary layer. The near-body grids are then embedded inside off-body Cartesian grids that extend to the far field.

By using a trimmed approach, hole-cutting is not needed on surface grids. Hole cutting is still required with the Cartesian off-body volume grids and between near-body volume grids. In this study, the X-ray hole cutting method is used. An X-ray object is created for every component in the geometry (i.e., the blades, the airframe, the landing gear, etc.). The user has to supply the list of meshes that each X-ray object is allowed to cut and an offset distance with which to grow each hole away

from the body. The hole cutting process is performed at each time step within the flow solver, in order to be able to solve the flow with a rotating geometry as in the case of rotors.

Near-body overset grids

The geometries for the Elytron 4S UAV, the prop-rotors, and the nose fan have been provided by Elytron Aircraft LLC to NASA Ames as a STL CAD triangulation. They can be imported directly into CGT, and then the overset grids are generated.

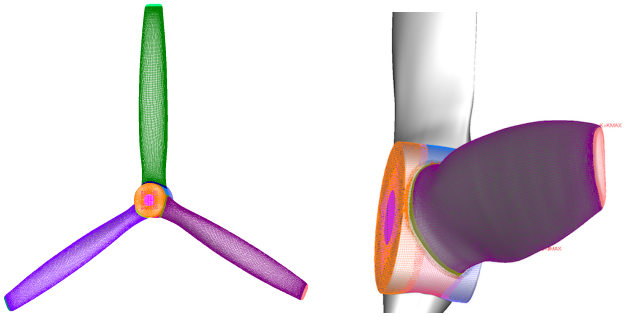

(a) Propeller, front view. (b) Blade of the prop-rotor.

Fig. 3. Elytron 4S UAV overset surface grids for a propeller, close-up view.

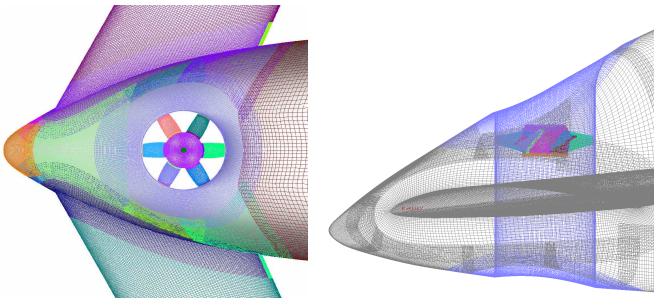

(a) Nose fan, top view. (b) Nose fan, side view.

Fig. 4. Elytron 4S UAV overset surface grids for nose fan and uncovered hole, close-up view.

The Elytron prop-rotor grid system consists of three blades attached to a central hub. O-grids are used for the blades. Cap grids are generated for the blade tips and the hub ends. In the blade-hub junctions, collar grids are employed. The rotor blade has a radius of $R_{tip} = 0.18\ m$ and a tip chord of $c_{tip} = 0.016\ m$, approximately. Figure 3 shows the propeller overset surface grids. The nose fan grids consist of six blades attached to a hub. O-grids are used for the blades. Cap grids are generated for the blade tips and the hub ends. In the blade-hub junctions, collar grids are employed. The nose fan blades have a radius of $R_{tip} = 0.04\ m$ and a tip chord of $c_{tip} = 0.016\ m$. Figure 4 shows the surface grids for the nose fan and hole. In the wing-fuselage junction, wing-winglet junctions, and wing-vertical empennage junction, collar grids are employed. O-grids have been used for all wings with high clustering around the trailing edge in order to solve the wakes and high clustering at the leading edge to accurately represent the curvature changes. The grid spacing normal to solid surfaces is such that $y^+ < 1$.

The wingspan for the fixed wings is $b_{fix} = 1.66\ m$, the wingspan for the tilt-wing is $b_{tilt} = 1.0\ m$, and the length of the tear-drop fuselage is $L = 1.35\ m$.

Four different geometric configurations are generated for the Elytron 4S UAV, in order to study the effect of different key components such as the propellers, the hole, and the fan. Figure 5 shows the four geometries.

I. Covered hole, without nose fan, without prop-rotors, the *glider*.

II. Uncovered hole, without nose fan, without prop-rotors, the *glider with hole*.

III. Uncovered hole, without nose fan, with prop-rotors, *powered without fan*.

IV. Uncovered hole, with nose fan, with prop-rotors, *powered with fan*.

Case IV represents the actual geometry of the wind-tunnel scaled model. This case will be simulated in forward flight with a static fan and the tilt-wings in airplane mode (tilt angle 0°), and in VTOL out of ground effect with the tilt-wings in helicopter mode (tilt angle 90°), in this case with the fan rotating for pitch control. In both cases the propellers rotate.

Off-body overset grids

Off-body Cartesian grids with uniform spacing surround the near-body grids to resolve the wake region of interest, see Figure 6. Multiple refinement levels of Cartesian grids efficiently expand the grid system to the far field, where each successive Cartesian grid is twice as coarse as its previous neighbor. The far-field boundary is 25 rotor radii away from the center of the vehicle in all directions. The resolved wake region has a uniform grid spacing of 10% of the tip chord length c_{tip}.

Table 1 sums up the characteristics of the grid systems for the four cases of this study. Case I, or the *glider*, has 88 near-body grids and a total of 183 grids, with 158 million grid points. Case II, or the *glider with hole*, has 87 near-body grids and 183 near-body and off-body grids, with 160 million grid points. For case III, or *powered without fan*, there are 119 near-body grids and a total of 244 grids for the near-body and off-body system. There are 357 million grid points. Finally, case IV, or *powered with fan*, has 147 near-body grids and 272 total grids. There are 361 million grid points.

The propellers double the number of points in the system, as the grids have to be refined in order to capture their wakes.

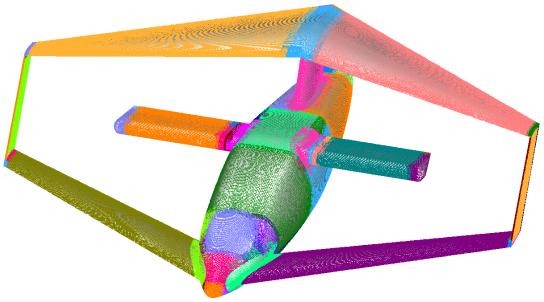

(a) Case I, oblique view.

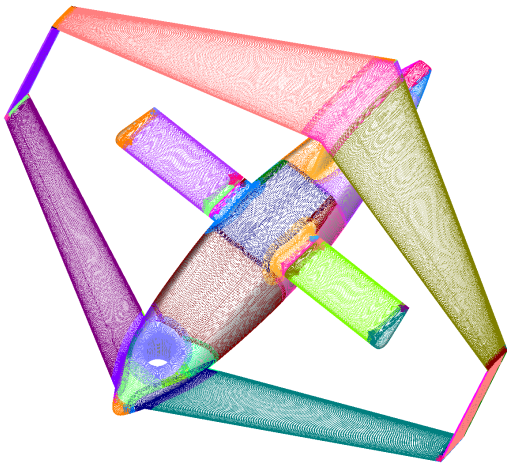

(b) Case II, view from above.

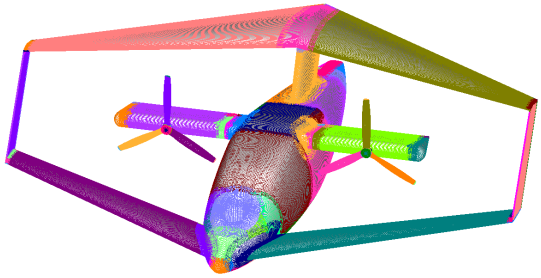

(c) Case III, oblique view.

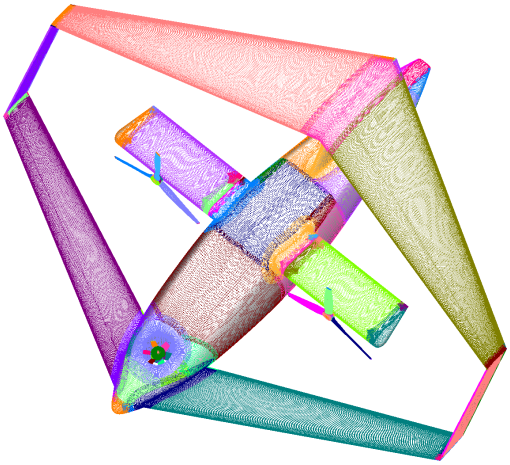

(d) Case IV, view from above.

Fig. 5. Elytron 4S UAV overset surface grids.

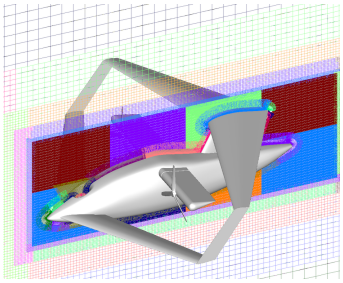

(a) Near field view.

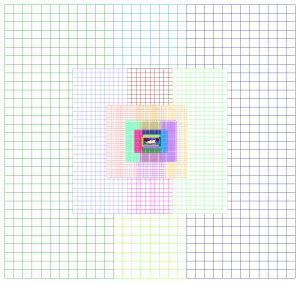

(b) Far field view.

Fig. 6. Elytron 4S UAV OB Cartesian grids for case IV. The surface geometry in grey-shaded, and a cut of all volume grids with plane $y = 0$ are shown.

Table 1. Elytron 4S UAV overset grids.

Case	NB+OB grids	Million grid points
Glider	183	158
Glider with hole	183	160
Powered without fan	244	357
Powered with fan	272	361

High-Order Accurate Navier-Stokes Solver

The Navier-Stokes equations can be solved using finite differences with a variety of numerical algorithms and turbulence models. In this study, the diagonal central difference algorithm is used with the 4^{th}-order accurate spatial differencing option with matrix dissipation or 5^{th}-order accurate spatial differencing option with scalar dissipation. The physical time step corresponds to 0.25 degree rotor rotation, together with up to 50 dual-time sub-iterations for a 2.5 to 3.0 orders of magnitude drop in sub-iteration residual. This numerical approach and time step were previously validated for various rotor flows (Refs. 8, 9). In order to reduce the computation time required for a converged solution, the first 1440 steps employ a time step equivalent to 2.5°per time step, yielding 10 rotor revolutions. The time step is then reduced to the equivalent of 0.25°per time step, for which 1440 steps correspond to one rotor revolution.

Hybrid turbulence modeling

The OVERFLOW code has a choice of algebraic, one-equation, and two-equation turbulence models (Ref. 4), including hybrid Reynolds-Averaged Navier-Stokes/Large Eddy Simulation (RANS/LES) models that close the RANS equations.

In this study for the Elytron 4S UAV, the one equation Spalart-Allmaras (Ref. 10) turbulence model is used primarily within the boundary layer.

The turbulence length scale, d, is defined as the distance from a field point to the nearest wall. A problem occurs deep within the rotor wake, where d may be several rotor radii in length. In this case, d no longer represents an estimate of the largest

turbulent eddy in the local flow but is rather a very large geometric parameter. When d is very large the turbulence dissipation becomes very small. On the other hand, the strong tip vortices in the lower wake can generate significant turbulence production. Over time, this imbalance in turbulence production and dissipation in the lower wake can result in excessively large eddy viscosities. These large viscosities can migrate up the vortex wake after several rotor revolutions and, under blade-vortex interaction conditions, infiltrate the blade boundary layers. When this happens, the rotor blade drag and torque increase significantly and artificially, resulting in an under-prediction of rotor efficiency.

An additional degree of realism can be obtained by the use of Large Eddy Simulation (LES). In LES, the large turbulent scales are resolved using a small grid spacing Δ, and the smaller scales are modeled. A low-pass spatial filter is applied to the Navier-Stokes equations, associated with a cut-off length. Below the cut-off length the subgrid-scales (SGS) must be modeled. However, the use of LES through the entire computational domain is impractical for the Reynolds numbers found in common rotor flows. This is due to the very small length scales of wall-bounded flows.

The Detached Eddy Simulation (DES) model (Ref. 10) is a more practical alternative. The intent of DES is to be in RANS mode throughout the boundary layer, where the turbulent scales can be very small and need to be modeled, and in LES mode outside the boundary layer where the largest turbulent scales are grid-resolved. In this way, DES is a RANS/LES hybrid approach that mitigates the problem of artificially large eddy viscosity. The turbulence length scale d is replaced by $\overline{d}$, where $\overline{d}$ is the minimum of the distance from the wall d and the local grid spacing times a coefficient.

The DES approach assumes that the wall-parallel grid spacing $\Delta_{\|}$ exceeds the thickness of the boundary layer δ so that the RANS model remains active near solid surfaces. If the wall-parallel grid spacing is smaller than the boundary layer thickness, $\Delta_{\|} < \delta$, then the DES Reynolds stresses can become under-resolved within the boundary layer, and this may lead to non-physical results, including grid-induced separation. Using Delayed Detached Eddy Simulation (DDES) (Ref. 11), the RANS mode is prolonged and is fully active within the boundary layer. The wall-parallel grid spacing used in this study does not violate the hybrid-LES validity condition; thus DES and DDES should give similar results. Nevertheless, all computations have been performed using the DDES model for both NB and OB grids.

Joined Wings

The box joined wing configuration in the Elytron 4S UAV is composed of the forward wing, the aft wing, and the winglets. The box-wing name comes from the box shape of the vehicle when looking from the front; see Figure 7. Prandtl investigated the theoretical advantages of the box-wing configuration in terms of induced drag reduction in (Ref. 12). In (Ref. 13), investigations on structural design, flight mechanics and dynamics, and wind tunnel tests showed that a smart design was needed to fully exploit the potential benefits of the joined wing design. In the following paragraphs, we will highlight some of the analysis by Wolkovitch from (Ref. 13).

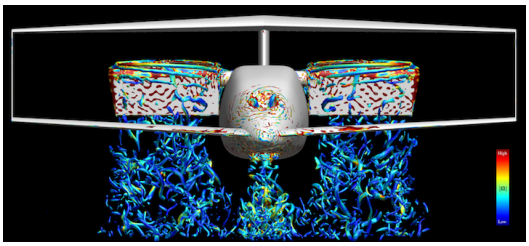

Fig. 7. Elytron 4S UAV, a box-wing configuration, during VTOL out of ground effect, viewed from the front. Q-criterion vorticity iso-surfaces colored by the vorticity magnitude.

Advantages claimed for the joined wing include:

- Light weight
- High stiffness
- Low induced drag

Some disadvantages are:

- Increased parasitic drag
- Buckling of the aft wing
- Aeroelastic instabilities

Joined wings are not invariably lighter than aerodynamically equivalent conventional wing-plus-tail systems. Weight will be only saved if:

- The geometrical parameters of the joined wing such as sweep, dihedral, and joint location are properly chosen.
- The internal wing structure is optimized.

In general, the forward and aft wings of a joined wing both lift upward. Thus, the fuselage is supported near both ends. By contrast, a conventional wing-plus-tail system supports the fuselage near the middle, with the tail applying a trimming download. The net result is that the fuselage bending moments produced by a joined wing are smaller than those produced by a comparable wing-plus-tail. Lateral and torsional fuselage loads may also be reduced since the joined wing provides additional load paths to withstand rolling and yawing moments applied by gusts or by control surfaces.

Under positive load factors, the rear wing of a joined wing pair is in compression. Therefore, overall column buckling must be considered. Box-wings present natural modes with low frequencies. The aeroelastic properties of box-wings seem to be strongly correlated with rigid (flight mechanics) modes.

Moreover, it seems that buckling and aeroelastic instabilities are coupled (Ref. 3).

The induced drag is reduced in the box-wing design when compared to the classic wing-plus-tail configuration. The wingtip vortices generated are weaker because there is no direct air flow from the lower surface of the wing to the upper surface at the tip, as both wings are joined through the winglets. The trailing wingtip vortices are responsible for the component of the downwash that creates induced drag. Still, because of the joined wing configuration, the supposed wingtip vortices are smaller than in a classical wing configuration. However, the wetted surface of a box-wing is larger when compared to a wing-plus-tail system, and therefore the parasitic drag is more important. The total drag may be reduced in the box-wing aircraft if the induced drag is minimum. It has been proved by many authors that there is more than one induced drag minimum in a box-wing configuration (Ref. 3).

In this study only the aerodynamics of the box-wing configuration of the Elytron is analyzed, by using high-fidelity CFD. The structures and aeroelasticity analysis of the Elytron 4S UAV are left for future work.

RESULTS

The OVERFLOW Navier-Stokes CFD code is used throughout this study. All CFD computations were carried out with NASA's supercomputers Pleiades and Electra located at the NASA Advanced Supercomputing (NAS) facilities at NASA Ames Research Center.

The Elytron 4S UAV has been simulated in forward flight, with the tilt-wing in "airplane mode" (tilt angle 0°), and in VTOL out of ground effect, with the tilt-wing in "helicopter-mode" (tilt angle 90°). Table 2 shows the different flight conditions tested in the wind tunnel.

Table 2. Elytron 4S UAV flight conditions tested in wind tunnel.

Flight mode	Forward flight	VTOL
N_{FAN} $[rpm]$	0	37000
N_{PROP} $[rpm]$	5800, 6500, 7200	9000
AoA [°]	0, 2.5, 5, 7.5, 10	0
V_∞ $[ft/s]$	67	0
Tilt angle [°]	0	90

In this study, we are showing the CFD results using OVERFLOW for the following flight conditions:

- Forward flight, with a freestream velocity $V_\infty = 67\ ft/s$, a static fan $N_{FAN} = 0$ rpm, for medium and high propeller rotational velocities $N_{PROP} = 6500$ rpm and $N_{PROP} = 7200$ rpm, and for angles of attack of AoA= 0° and AoA= 10°.
- Vertical Take-Off and Landing (VTOL) out of ground effect, with a propeller rotational velocity of $N_{PROP} = 9000$ rpm and a fan rotational velocity of $N_{FAN} = 37000$ rpm.

The design of the box-wing reduces the induced drag and enhances structural stiffness. The effect of having joined wings with oversized winglets decreases the wingtip vortices and creates a larger effective aspect ratio, reducing the drag. With the tilt-wing concept, there is no retreating blade problem as in the helicopter rotor blades in forward flight. This allows the vehicle to fly faster as the rotor blade will not suffer from dynamic stall.

Case I, the glider

The geometry for case I or the *glider* (covered hole, without nose fan, without prop-rotors) has been simulated in forward flight for an anlge of attack AoA= 0° and a freestream velocity $V_\infty = 67 ft/s$. This case represents the clean aircraft, with no propulsion. Figure 8 shows the pressure at the surface of the vehicle, and the Q-criterion vorticity iso-surfaces, where blue represents the lowest pressure and red the highest pressure. Warmer colors represent higher pressures than colder colors. The turbulent flow structures can be observed in the figures using Q-criterion vorticity iso-surfaces, which show the cores of the vortices.

The complicated configuration of the Elytron with a joined wing, empennage, and tilt-wing with its multiple junctures, is the source of many vortices:

- Wingtip vortices at the junction of the winglet with the aft wing.
- Wingtip vortices at the junction of the winglet with the forward wing.
- Wingtip vortices at the tip of the tilt-wing.
- Vortices at the junction of the tilt-wing with the fuselage.
- Vortices at the junction of the empennage with the aft wing.
- Horseshoe vortices at the junction of the forward wing, the tilt-wing, and the empennage with the fuselage.

A wingtip vortex is generated at the tip of the wing due to the difference in pressure between the lower surface (pressure side) and the upper surface (suction side). Air flows from below the wing and out around the tip to the upper surface of the wing in a circular fashion, producing the wingtip vortex. In fact, according to lifting-line theory, vorticity is trailed at any point on the wing where the lift varies span-wise; it eventually rolls up into large vortices near the wingtip, at the edge of flap devices or at other abrupt changes in wing planform. That is, a vortex is generated whenever there is a change in lift span-wise. Wingtip vortices at the aft and forward wings are due to the change in lift close to the tip. The strength of the vortex at the tip of the tilt-wing is relatively weak and is not visible in the figures.

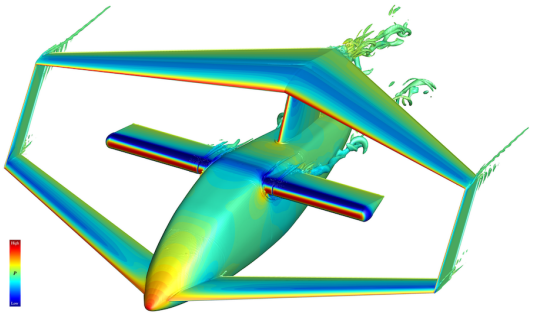

(a) Oblique view.

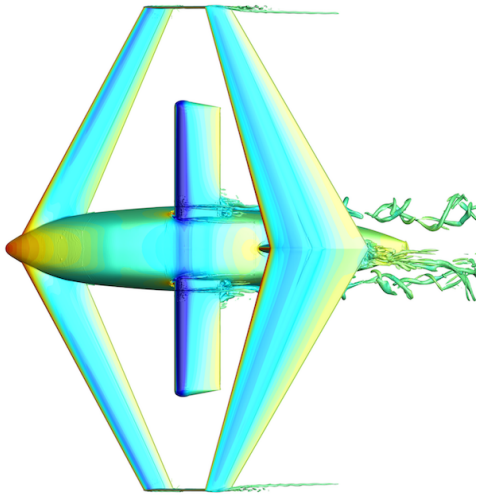

(b) Top view.

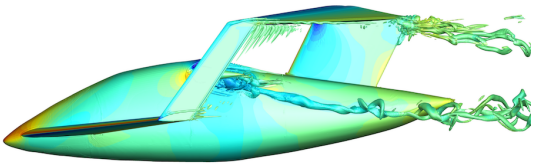

(c) Side view.

Fig. 8. Q-criterion vorticity iso-surfaces and body surface pressure in forward flight at AoA$= 0^\circ$ and $V_\infty = 67\ ft/s$ for the Elytron 4S UAV, grid system I, the *glider*.

The vortices at the juncture of the tilt-wing with the fuselage are possibly caused by the horseshoe vortices of the junction and the small gap between the two wing sections. This small gap between the two sections of the tilt-wing is left in order to rotate the tilt-wing to transition from VTOL to forward flight and vice versa.

Vortices are generated at the complicated juncture of the empennage with the aft wing; Figure 9 shows in detail the complicated juncture of the empennage with the aft wing, the pressure at the surface of the Elytron, and the Mach number contours. Small grid cells and many surface grids were required to accurately represent this section of the design. The background picture shows a view of the Elytron from the back, with the surface mesh and pressure at the body surface.

Horseshoe vortices are usually generated at the junction of the

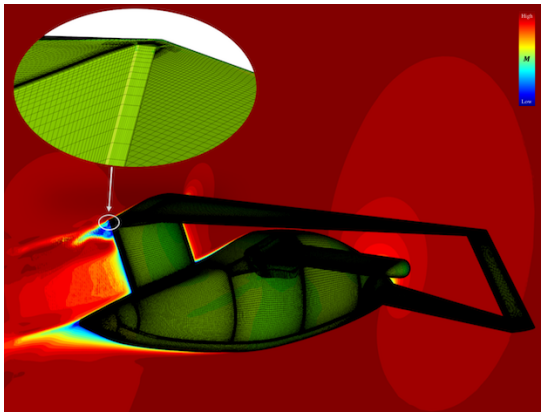

Fig. 9. A close-up view of the junctions of the empennage with the aft wing. The slice shows the Mach number contours.

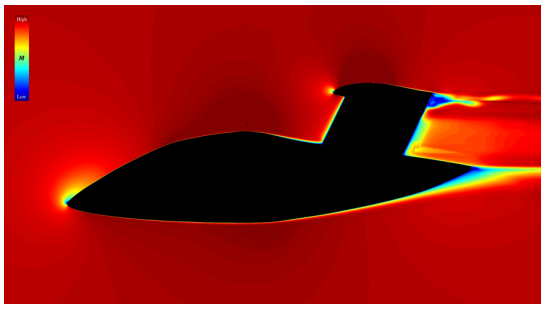

Fig. 10. Mach number in forward flight at AoA$= 0^\circ$ and $M_\infty = 0.06$ of the Elytron 4S UAV, grid system I, the *glider*.

wing with the fuselage because of the change of lift span-wise, and, according to lifting-line theory, a change in lift span-wise will trail vortices. At the junction of the wing with the fuselage, the lift drops at the fuselage.

As the angle of attack is equal to AoA$= 0^\circ$, the lift generated is positive but close to zero. Increasing the angle of attack will increase the lift, and in consequence the induced drag will increase too. As has been mentioned in the joined wing section, a box-wing greatly decreases the induced drag because the wingtip vortex is weaker or almost inexistent. However, the simulations show the formation of wingtip vortices, which contribute to the induced drag. These vortices get stronger when we increase the angle of attack, as described in the following paragraphs. Figure 10 shows the Mach number contours at a slice $y = 0$, where the blue regions indicate velocity close to zero. As the fuselage has an aerodynamic shape, the air flows smoothly around it.

Case II, the glider with hole

In this case, we add a hole close to the nose, where the nose fan can be placed. We want to see the changes in the flow caused by the empty hole, for the same flow conditions as in case I, that is, forward flight with an angle of attack AoA$= 0^\circ$ and freestream velocity $V_\infty = 67 ft/s$. Note that the hole is empty for this case.

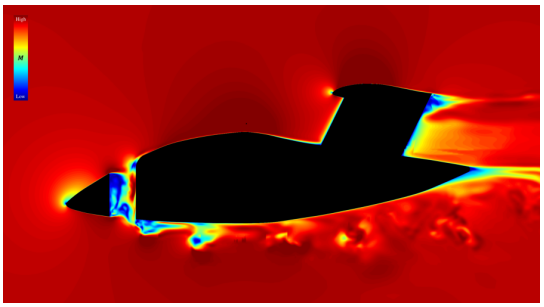

Fig. 11. Mach number in forward flight at AoA$= 0^\circ$ and $M_\infty = 0.06$ of the Elytron 4S UAV, grid system II, the *glider with hole*.

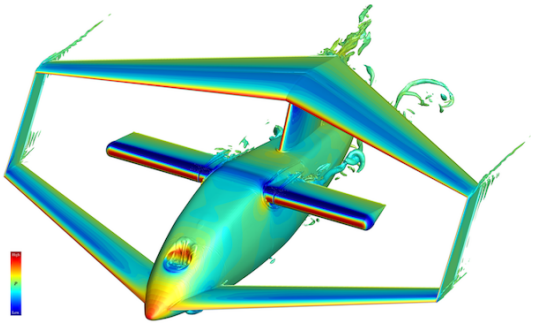

(a) Oblique view.

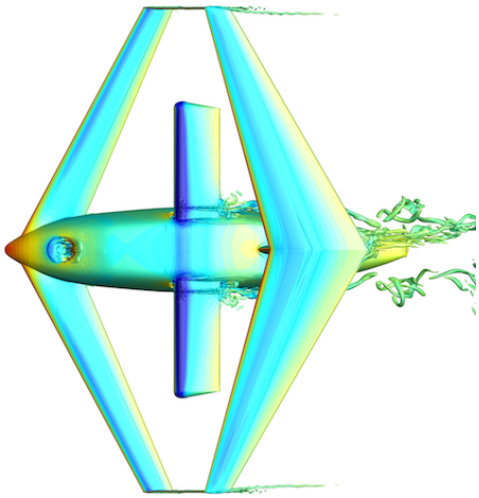

(b) Top view.

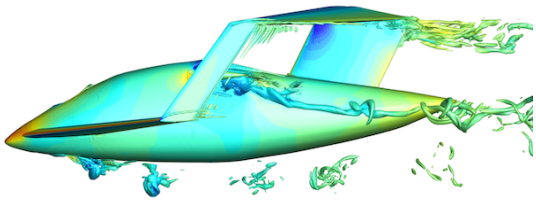

(c) Side view.

Fig. 12. Q-criterion vorticity iso-surfaces and body surface pressure in forward flight at AoA$= 0^\circ$ and $V_\infty = 67\ ft/s$ for the Elytron 4S UAV, grid system II, the *glider with hole*.

Figure 11 shows the Mach number in a slice at $y = 0$, where the Elytron surface has been hidden in order to easily see the interior of the hole. The freestream Mach number is $M_\infty = 0.06$. The hole generates unsteady flow fluctuations inside. Some flow is spilled outside the hole, as seen by the shedding vortices below the fuselage.

Figure 12 shows the Q-criterion vorticity iso-surfaces and the pressure at the surface. The same vortices as in case I can be observed in this figure: the wingtip vortices from the aft and forward wings, relatively weak; the vortices from the junction of the tilt-wing with the fuselage and the gap, more important; and the vortices from the juncture of the empennage and the aft wing. As has been mentioned previously, the hole produces vortex shedding underneath the fuselage.

Case III, powered without fan

For this case, the propellers are added to the tilt-wings, and the hole remains empty. The propellers rotate in the high regime, $N_{\text{PROP}} = 7200$ rpm. For this geometry, two angles of attack are studied, AoA$= 0^\circ$, shown in Figure 14, and AoA$= 10^\circ$, shown in Figure 15.

The propellers are the source of thrust in a rotorcraft. The two previous cases with the glider were an abstraction of reality, as every aircraft needs propulsion in order to maintain a steady flight. However, they are still useful to simulate and analyze in order to understand the junction-flows, without the effects of the propellers for example.

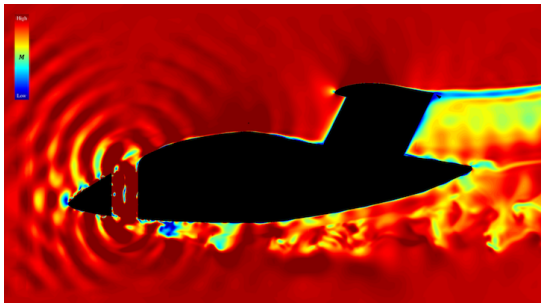

(a) AoA$= 0^\circ$.

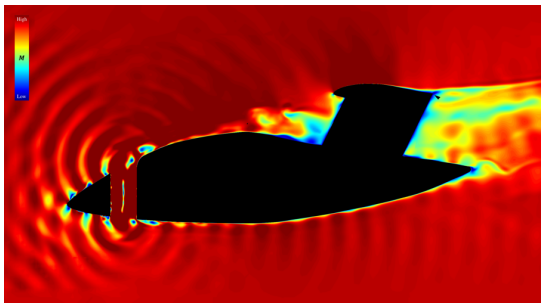

(b) AoA$= 10^\circ$.

Fig. 13. Mach number in forward flight at $M_\infty = 0.06$ of the Elytron 4S UAV, grid system III, *powered without fan*.

A vortex generated at the tip of the blade of a propeller is called the bladetip vortex. This vortex can interact with the

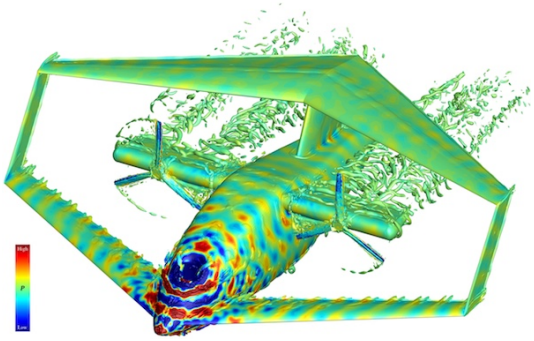

(a) Oblique view.

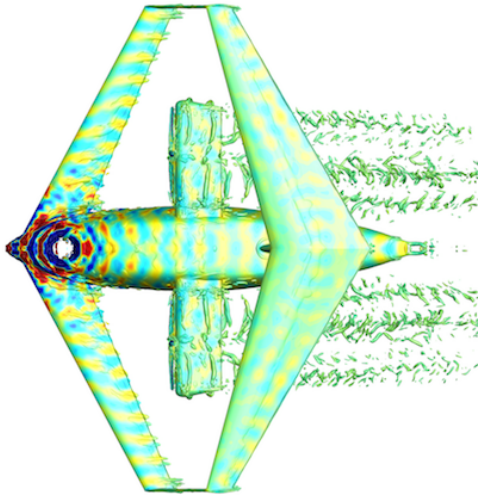

(b) Top view.

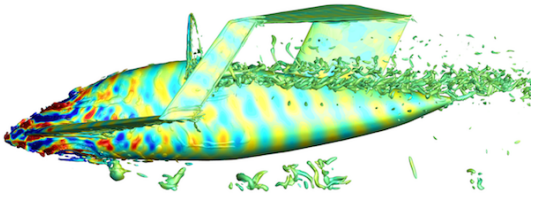

(c) Side view.

Fig. 14. Q-criterion vorticity iso-surfaces and body surface pressure in forward flight at AoA$= 0°$, $V_\infty = 67\ ft/s$ and $N_{\mathbf{PROP}} = 7200$ rpm for the Elytron 4S UAV, grid system III, *powered without fan*.

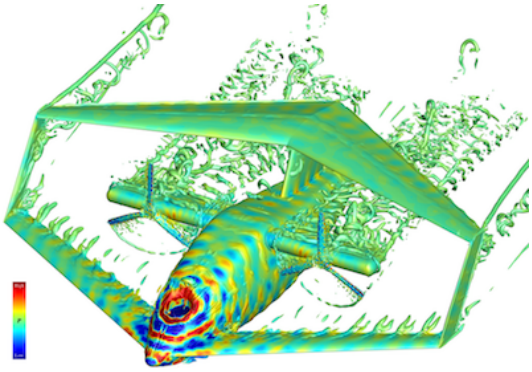

(a) Oblique view.

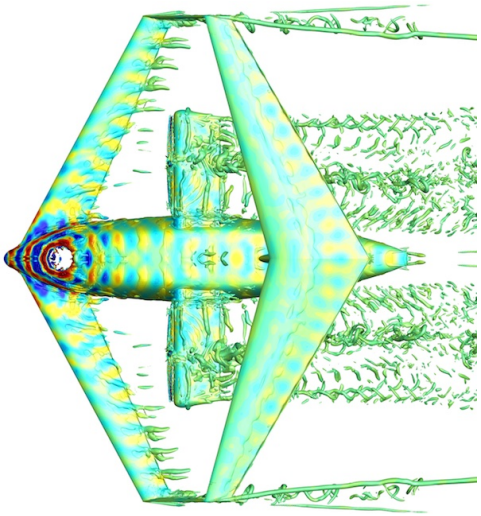

(b) Top view.

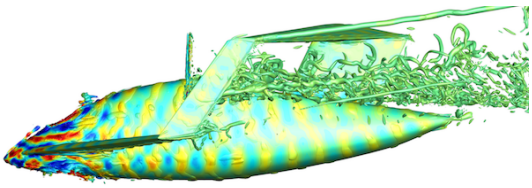

(c) Side view.

Fig. 15. Q-criterion vorticity iso-surfaces and body surface pressure in forward flight at AoA$= 10°$, $V_\infty = 67\ ft/s$ and $N_{\mathbf{PROP}} = 7200$ rpm for the Elytron 4S UAV, grid system III, *powered without fan*.

next incoming blade, producing what is called Blade-Vortex Interaction (BVI). That is, BVI occurs when a rotor blade passes within a close proximity of the shed tip vortices from a previous blade. This causes a rapid, impulsive change in the loading on the blade resulting in the generation of highly directional impulsive loading noise.

For the Elytron in forward flight with the tilt-wing in airplane mode, there are no retreating blade problems[1]. The bladetip vortices interact with the tilt-wing and go downstream. BVI is not very important, as the vortices are carried downstream by the freestream velocity and do not interact with the following blade.

The hole is the source of very strong pressure fluctuations; see the frequent red and blue regions on the fuselage. These strong fluctuations may lead to vibrations and instabilities. Adding the propellers to the vehicle while leaving the hole

[1]Retreating blade stall is a hazardous and damaging flight condition in helicopters, where the rotor blade on the retreating side of the rotor disc in forward flight, and therefore with the smaller resultant relative wind, exceeds the critical angle of attack. Retreating blade stall is one of the primary limiting factors in a helicopter's airspeed and the reason even the fastest helicopters can only fly slightly faster than 200 knots.

empty is not a good configuration. However, the wingtip vortices for AoA= 0° have almost disappeared, this shows that the joined wing design works. If the angle of attack increases to AoA= 10°, the vorticity is relatively stronger everywhere, the lift increases, and so does the induced drag. The wingtip vortices are very clear now. This box-wing has not been designed for flying at high angles of attack, and that's the reason why, for AoA= 10°, the wingtip vortices are visible.

The wingtip vortex from the junction aft wing winglet goes downstream and inboard (towards the symmetry axis), and the wingtip vortex from the junction front-wing winglet goes downstream and outboard (away from the symmetry axis). This is probably due to suction from the propeller's vortex wake, closer to the aft wing wingtip vortices than to those of the forward wing.

At an angle of attack AoA= 0° there is vortex shedding from the hole below the fuselage and very strong pressure fluctuations, as can be seen in Figures 13(a) and 14. The turbulent structures observed with the Q-criterion vorticity show vortex shedding: vortices are emitted from the hole underneath the fuselage periodically.

For an angle of attack of AoA= 10°, the flow is contained inside the hole as seen in Figure 13 (b), but it fluctuates inside and produces the propagation of strong pressure waves. Looking closely at the side view, it seems that for AoA= 10° some vortices are generated at the hole and emitted above the fuselage. The airfoil pressure distributions from different sections of the wing are greatly affected by the pressure fluctuations coming from the hole, modifying the lift distribution of the wing and emitting many vortices from these sections. The pressure disturbances from the hole are stronger for small angles of attack, but more vortices are observed for AoA= 10°.

The vortex wake from the propellers is deflected down by the aft wing; this effect is more important for higher angles of attack. The deflection of the wake generates a nose-up pitch moment, which gets stronger as we increase the AoA. In order to be stable, this nose-up moment has to be compensated with active control surfaces, placed for example on the tilt-wings.

Case IV, powered with fan

This case represents the real geometry of the model tested in the wind tunnel. A nose fan is placed in the hole for pitch control and load balancing during VTOL. In forward flight, the nose fan is static. Figure 17 shows the Q-criterion vorticity iso-surfaces and the pressure at the surface for flight conditions AoA= 0°, $V_\infty = 67\ ft/s$, $N_{\text{PROP}} = 6500$ rpm and $N_{\text{FAN}} = 0$ rpm. Figure 18 shows the Q-criterion vorticity iso-surfaces and the pressure at the surface for the same flight conditions and AoA= 10°. For this case, we show the propellers rotating at medium velocity, but the flow disturbances and downwash from the propellers should be similar to those in case III with high rotational velocity.

The non-rotating fan is partially blocking the hole effect. Figure 16 shows the Mach number M on a slice at $y = 0$, where

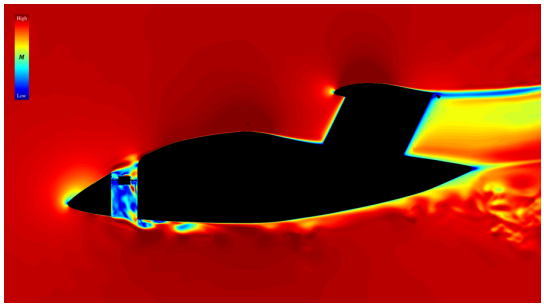

(a) AoA= 0°.

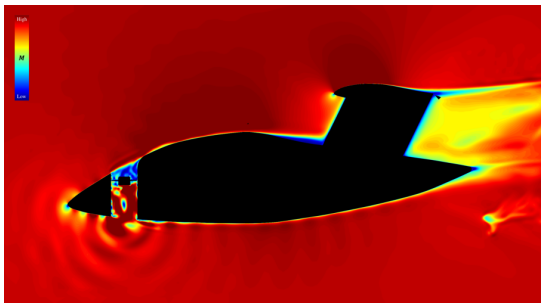

(b) AoA= 10°.

Fig. 16. Mach number in forward flight at $M_\infty = 0.06$ of the Elytron 4S UAV, grid system IV, *powered with fan*.

the surface of the Elytron has been hidden in order to visualize clearly the interior of the hole, for AoA= 0° and AoA= 10°.

As in case III, the wingtip vortices are relatively weak for AoA= 0°, thanks to the joined wing design. But, again, the wingtip vortices are more important for an AoA= 10°. The wingtip vortices at the junctions of the aft wing-winglets are relatively stronger than those at the junctions of the forward wing-winglets.

At an AoA= 0° the air flow inside the hole is partially blocked thanks to the static fan, but there is still vortex shedding underneath the fuselage, as seen in Figures 16 (a) and 17 (c). In this case, with a static fan inside the hole, the pressure fluctuations are smaller than those without a fan blocking the flow (the *powered without fan* Elytron case). The static fan reduces the disturbances.

For an angle of attack of AoA= 10°, the flow inside the hole is almost totally blocked, as seen in Figure 16 (b) by the low velocity region above the fan. However, inside the hole, below the fan, the flow is contained but it fluctuates, generating the propagation of pressure waves. The fluctuations are stronger than for AoA= 0°. In addition, as flow through the hole is almost totally blocked by the static fan, flow is spilled out of it above the fuselage, producing vortices, as seen in the side view of Figure 18.

Case IV, powered with fan in VTOL out of ground effect

Figure 19 shows the rotor wakes and the instantaneous surface pressure on the body for the Elytron 4S UAV in VTOL out of ground effect. The conditions simulated have the

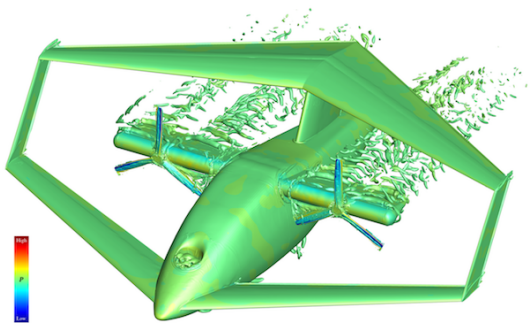

(a) Oblique view.

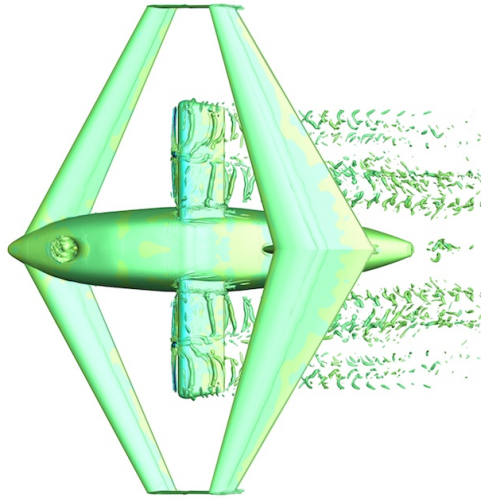

(b) Top view.

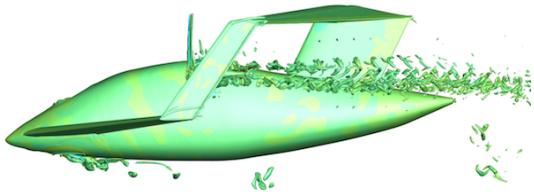

(c) Side view.

Fig. 17. Q-criterion vorticity iso-surfaces and body surface pressure in forward flight at AoA$= 0°$, $V_\infty = 67\ ft/s$, $N_{\mathbf{PROP}} = 7200$ rpm and $N_{\mathbf{FAN}} = 0$ rpm for the Elytron 4S UAV, grid system IV, *powered with fan*.

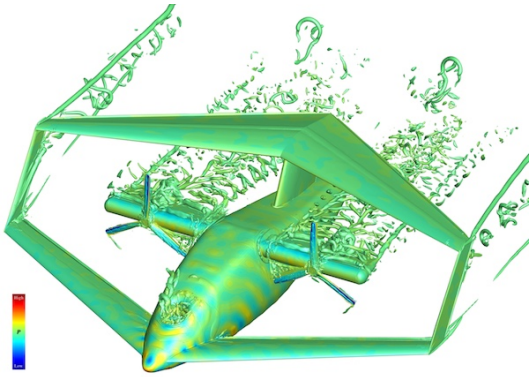

(a) Oblique view.

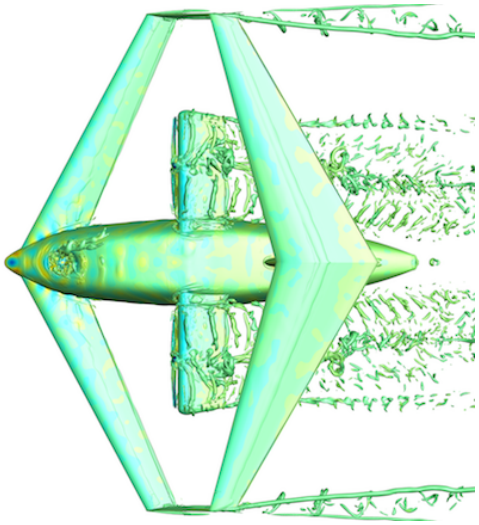

(b) Top view.

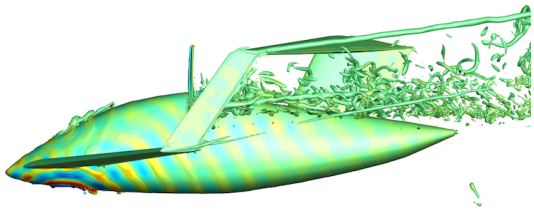

(c) Side view.

Fig. 18. Q-criterion vorticity iso-surfaces and body surface pressure in forward flight at AoA$= 10°$, $V_\infty = 67\ ft/s$, $N_{\mathbf{PROP}} = 7200$ rpm and $N_{\mathbf{FAN}} = 0$ rpm for the Elytron 4S UAV, grid system IV, *powered with fan*.

propellers and fan rotating at maximum rotational velocity, $N_{\mathrm{PROP}} = 9000$ rpm and $N_{\mathrm{FAN}} = 37000$ rpm. During take-off and landing, the tilt-wing is tilted $90°$ for VTOL.

With the wing in helicopter mode and no freestream velocity, there is BVI. The vortices shed from the previous blade pass very close to the next blade. This causes a rapid change in the loading of the blade, producing noise. Also, the vortices interact further downstream with the tilt-wing, which is immersed in their wake, creating another source of noise. The cabin must be very well sound-insulated in order to be able to carry passengers.

The nose fan high rotational velocity produces high frequency pressure fluctuations, as seen in Figure 19. In this figure one can also clearly see the vortex wakes from the nose fan and the propellers.

Figure 20 shows the Mach number contours at $y = 0$ and at $x = constant$ slices. They show the downwash velocities of the propellers and the nose fan. The tilt-wing generates less download force than a tilt-rotor like the XV-15 or the V-22 while in hover.

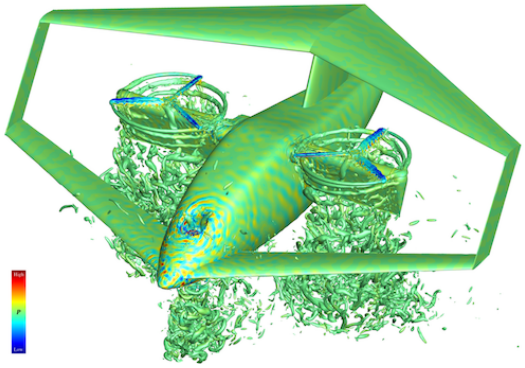

(a) Oblique view.

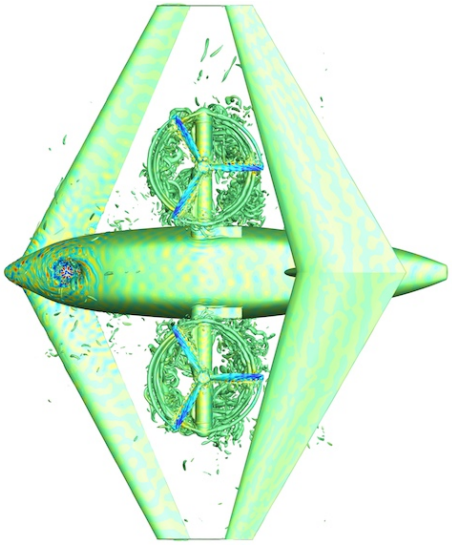

(b) Top view.

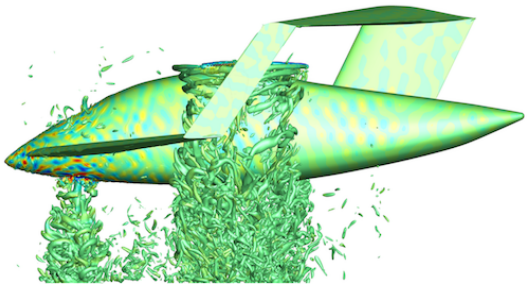

(c) Side view.

Fig. 19. Q-criterion vorticity iso-surfaces and body surface pressure in VTOL out of ground effect at AoA$= 0^\circ$, $V_\infty = 0\ ft/s$, $N_{\mathbf{PROP}} = 9000$ rpm and $N_{\mathbf{FAN}} = 37000$ rpm for the Elytron 4S UAV, grid system IV, *powered with fan*. The tilt-wings are tilted 90° so the thrust from the propellers is vertical.

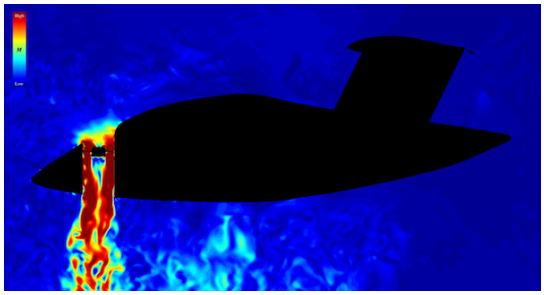

(a) $y = 0$ slice.

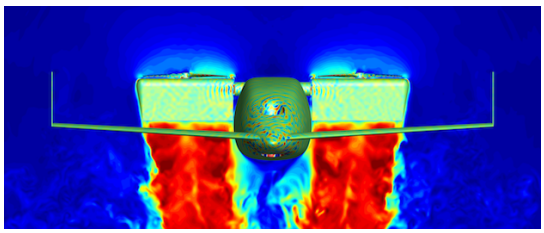

(b) $x = constant$ slice.

Fig. 20. Mach number in VTOL out of ground effect at $M_\infty = 0.06$ of the Elytron 4S UAV, grid system IV, *powered with fan*.

SUMMARY AND FUTURE WORK

High-order accurate Computational Fluid Dynamics simulations have been carried out for the Elytron 4S UAV. NASA's supercomputers Pleiades and Electra were essential for this work as the overset grids have hundreds of millions of grid points. However, only one to two days were needed for converging the quasi-steady solutions using 1024-2048 processors; the solution converged after 30 rotor revolutions.

The Elytron 4S UAV is the UAV scaled model of the future Urban Air Mobility concept, the Elytron 4S. The innovative design of the Elytron included a tilt-wing for VTOL and a box-wing for reducing induced drag. The design of the box-wing reduces the induced drag and enhances structural stiffness. The effect of having joined wings with oversized winglets decreases the wingtip vortices and creates a larger effective aspect ratio, reducing the drag. With the tilt-wing concept, there is no retreating blade problem as in the helicopter rotor blades in forward flight. This allows the vehicle to fly faster as the rotor blade will not suffer from dynamic stall.

The Elytron 4S UAV has been simulated in forward flight for different flight conditions and geometries, with the tilt-wing in airplane mode (tilt angle 0°), and in VTOL, with the tilt-wing in helicopter mode (tilt angle 90°).

Even the glider in forward flight shows the formation of many vortices at the junctions of the components. Adding a hole to the glider system creates vortex shedding underneath the fuselage. When the propellers are placed in front of the tilt-wings while leaving the hole empty, in the powered without fan case, strong pressure fluctuations originate at the hole. Wingtip vortices for small angles of attack are relatively weak, but they get stronger as the angle of attack increases. Vortex shedding is

seen underneath the fuselage for AoA= 0° and over the fuselage for AoA= 10°. If a static fan is added inside the hole, the air flow is partially blocked through the hole, greatly reducing the pressure fluctuations.

In VTOL out of ground effect, the nose fan rotates at maximum velocity, producing high-frequency pressure fluctuations. The nose fan is used for pitch control, and BVI can be observed for the propeller blades.

In this study, only the aerodynamics has been analyzed; future work should study the structures and aeroelasticity of this innovative and complex configuration. New unconventional designs may lead to important improvements in terms of performance, but they should be carefully designed without omitting any field, to ensure truly safe vehicles.

Author contact:
Patricia Ventura Diaz, patricia.venturadiaz@nasa.gov.

ACKNOWLEDGEMENTS

This work was supported by the DELIVER (Colin Theodore, project manager) and RVLT (Susan Gorton, project manager) projects and utilized the Pleiades and Electra supercomputers at NASA's Advanced Supercomputing (NAS) Division. The authors would like to thank Thomas Pulliam, William Chan, Witold Koning, and Nagi N. Mansour for helpful discussions. Witold Koning provided the CAE STL model of the Elytron 4S UAV.

REFERENCES

[1]Yoon, S., Ventura Diaz, P., Boyd, D. D., Chan, W. M., and Theodore, C. R., *Computational Aerodynamic Modeling of Small Quadcopter Vehicles*, AHS Paper 73-2017-0015, The 73rd Annual AHS International Forum & Technology Display, Fort Worth, Texas, May 2017.

[2]Ventura Diaz, P. and Yoon, S., *High-Fidelity Computational Aerodynamics of Multi-Rotor Unmanned Aerial Vehicles*, AIAA Paper 2018, The AIAA SciTech Forum 2018, Kissimmee, Florida, Jan. 2018.

[3]Cavallaro, R. and Demasi, L., *Challenges, Ideas, and Innovations of Joined-Wing Configurations: A Concept from the Past, an Opportunity for the Future*, Progress in Aerospace Sciences 87 (2016), pp. 1-93.

[4]Nichols, R., Tramel, R., and Buning, P., *Solver and Turbulence Model Upgrades to OVERFLOW2 for Unsteady and High-Speed Flow Applications*, AIAA Paper 2006-2824, June 2006.

[5]Pulliam, T. H., *High Order Accurate Finite-Difference Methods: as seen in OVERFLOW*, AIAA Paper 2011-3851, June 2011.

[6]Chan, W. M., *Developments in Strategies and Software Tools for Overset Structured Grid Generation and Connectivity*, AIAA Paper 2011-3051, Honolulu, Hawaii, June 2011.

[7]Chan, W. M., Gomez, R. J., Rogers, S. E., Buning, P. G., *Best Practices in Overset Grid Generation*, AIAA Paper 2002-3191, St. Louis, Missouri, June 2002.

[8]Yoon, S., Lee, H. C., and Pulliam, T. H., *Computational Analysis of Multi-Rotor Flows*, AIAA Paper 2016-0812, The 54th AIAA Aerospace Sciences Meeting, San Diego, California, Jan. 2016.

[9]Yoon, S. Lee, H. C., and Pulliam, T. H., *Computational Study of Flow Interactions in Coaxial Rotors*, The AHS Technical Meeting on Aeromechanics Design for Vertical Lift, San Francisco, California, Jan. 2016.

[10]Spalart, P. R., Jou, W-H., Strelets, M., and Allmaras, S. R., *Comments on the Feasibility of LES for Wings and on a Hybrid RANS/LES Approach*, Advances in DNS/LES, Greyden Press, 1997, pp. 137-147.

[11]Spalart, P. R., *Strategies for Turbulence Modeling and Simulations*, International Journal of Heat and Fluid Flow, 21, 2000, pp. 252-263.

[12]Prandtl, L., *Induced Drag of Multiplanes*, Technical Report TN 182, NACA, reproduction of Der induzierte Widerstand con Mehrdeckern, Technische Ber. 3, 1918, pp. 309-315, Match 1924.

[13]Wolkovitch, J., *The Joined Wing: An Overview*, AIAA Paper 85-0274, The AIAA 23rd Aerospace Sciences Meeting, Reno, Nevada, January 1985.